J. Fluid Mech. (1988), *vol.* 187, *pp.* 115–140
Printed in Great Britain

Experimental and numerical investigation of a forced circular shear layer

By J. M. CHOMAZ, M. RABAUD
Groupe de Physique des Solides de l'Ecole Normale Supérieure,
24 rue Lhomond, 75005 Paris, France

C. BASDEVANT
Laboratoire de Météorologie Dynamique, Ecole Normale Supérieure,
24 rue Lhomond, 75005 Paris, France

AND Y. COUDER
Groupe de Physique des Solides de l'Ecole Normale Supérieure,
24 rue Lhomond, 75005 Paris, France

(Received 9 December 1986)

In a previous article we introduced a dissipative circular geometry in which stationary states of the shear flow instability were obtained. We show here that the dynamical behaviour of this flow depends strongly on the aspect ratio of the cell. In large cells, where the number of vortices is large, transitions from a mode with m vortices to a mode with $(m-1)$ vortices occur through localized processes. In contrast to that situation, in small cells, transition takes place after a series of bifurcations which correspond to the successive breaking of all the symmetries of the flow.

We show that, provided an adequate forcing term is introduced, a two-dimensional numerical simulation of this flow is sufficient to recover all the dynamical processes which characterize the experimental flow.

1. Introduction

A fluid submitted to a velocity shear is unstable, and tends to form a line of vortices which is itself unstable and evolves through vortex-pairing processes. The experimental description of this destabilization is difficult to compare with numerical simulations or theoretical models. This difficulty must be analysed briefly as it forms the framework for our results.

Unstable flows have been classified (Huerre & Monkevitz 1985) into two categories: absolutely unstable flows and convectively unstable flows. Absolutely unstable flows (e.g. Rayleigh–Bénard convection) are described by temporal stability calculations. In these cases, a local disturbance leads to the growth of the instability everywhere in the cell. In contrast, in convectively unstable flows (e.g. spatial shear layer) the disturbances, as they grow, are transported away by the mean flow at a velocity larger than the group velocity of any of the perturbations so that they cannot affect the flow upstream. A spatial theory of the instability is then necessary. This is one of the sources of difficulty in comparing the results of shear-flow experiments with either numerical simulations or theoretical modelling of rows of vortices. They often do not study the same kind of instability.

Most experiments on shear flows are performed in the mixing layer configuration

where two fluids come into contact at the end of a splitter plate with velocities such that the instability is of a convective type. A review of the results of such experiments can be found in Aref (1983) and Ho & Huerre (1984). After the appearance of small vortices, the shear-layer width grows downstream by pairing of vortices (Winant & Browand 1974). In general these pairings occur without correlation. These convective flows are sensitive to any external disturbances and act as selective noise amplifiers. It is only by applying a subharmonic excitation to the flow that Ho & Huang (1982) have been able to force systematic pairing of the vortices downstream. The convective property of the instability depends on the mean velocity of the two fluids. In a configuration where two fluids of different densities flow in opposite directions under the influence of gravity, Thorpe (1971) observes temporal instability and nearly simultaneous pairing of adjacent vortices.

Most of the numerical simulations studied the temporal growth of the instability in an initially spatially periodic, rectilinear, shear zone. In his critical review of the numerical simulations, Aref (1983) pointed out that most authors work in conditions where strong discretization allows only modes with very few vortices. These authors observe an ordered structure and tend to overestimate the genericity of this result. In other simulations where higher number of vortices could appear, the primary patterns are not perfectly periodic and pairings are uncorrelated.

From a theoretical point of view, the temporal linear analysis performed in the absolutely unstable case, gives a good prediction of the fastest growing wave in an unstable shear flow. As does the spatial theory for convective unstable mixing layers. However, the analysis fails to describe the increased concentration of vorticity in localized structures. For this reason many authors have chosen to study theoretically the properties of regular infinite rows of artificial vortices. In all the models, with point vortices (Lamb 1932), or with vorticity spread on a few finite areas (Stuart 1967; Pierrehumbert & Widnall 1982), the destabilization of the pattern occurs through the growth of the subharmonic wave which tends to lead to correlated pairings.

The results we present are obtained under conditions that are specific in the following three characteristics:

we work in a closed geometry with rotational invariance;

a dissipative process opposes the development of the instability, so that steady states of the vortex patterns are obtained under the control of an external parameter;

the circular geometry imposes a discretization of the possible modes.

For these three reasons, we will show that we obtain a situation where the experiment may be directly comparable with a numerical simulation.

In a previous article, two of us (Rabaud & Couder, 1983; hereinafter referred to as RC) presented the type of cell we use and reported the first results obtained in this geometry. Let us recall that the fluid is enclosed in a vertical cylinder of radius R_2 and very small height e (figure 1). A disk of radius R_1 at the centre of each end, rotates at angular velocity Ω_1, while the rest of the cell rotates at Ω_2. Viscous friction on the containing walls forces the fluid into two solid rotations at Ω_1 in the central part and Ω_2 in the external annulus respectively, separated by a shear zone. At low velocities an axisymmetric flow is observed. Above a well-defined threshold a pattern of vertical vortices shows up. The onset of the instability is characterized by a critical value Re_c of the Reynolds number

$$Re = \frac{|\Omega_2 - \Omega_1|}{\nu} R_1 e,$$

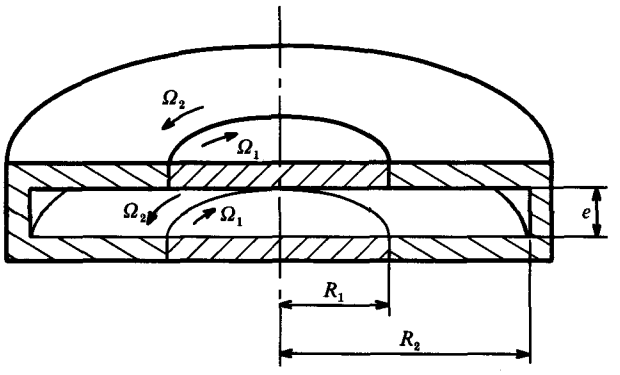

FIGURE 1. Sketch of the experimental cell.

where ν is the kinematic viscosity of the fluid. The pattern formed of m_c regular vortices can be characterized by its wave vector $k_c = m_c/R_1$.

Neither the centrifugal nor the Coriolis forces have an influence on this instability provided the cell thickness is smaller, or of the order of magnitude, of the Ekman layer thickness

$$h \approx \left(\frac{\nu}{|\Omega_2 - \Omega_1|}\right)^{\frac{1}{2}}$$

corresponding to the differential rotation.

RC also showed that a similar instability would be observed in a rectilinear geometry where the fluid would be enclosed in a rectangular tube of height e formed by two U-shaped parts moving in opposite directions. An analytic solution for the viscous flow can be found in this geometry. The typical width for the shear is maximum (and of the order of e) in the median plane of the cell where the damping due to friction on the walls is minimum, so that this is the most unstable region. A semi-quantitative model of the instability gives the right value of the unstable wavenumber k_c as well as an estimate of the value of the Reynolds number Re_c at the threshold. The vortex pattern at Re_c is stable if the velocities are kept constant. By increasing $|\Omega_2 - \Omega_1|$, the size of the vortices will grow and a series of transitions towards patterns with ever smaller numbers of vortices will take place. A sequence of modes with m_c, $m_c - 1$, $m_c - 2$ is then obtained.

The first aim of the present article is to report new results on the destabilization of the vortex patterns. In §2 we present the new experimental set-up, and in §3 we show that the destabilization of a pattern depends strongly upon the number m of vortices involved, and therefore for a given constraint upon the aspect ratio $\Gamma = R_1/e$ of the cell. In §3.4 we will briefly describe the limitation of this analysis.

Our second aim (§4) is to show how a two-dimensional numerical model, where a forcing term has been introduced, reproduces all the dynamical characteristics of the flow. Comparison between experimental and numerical results will extend to the onset of the instability, the selection of the wavenumber, the stability of the modes, and the transitory states. A short conclusion follows.

2. The experimental set-up

We used both the original cell of RC and an improved version. As the size of the vortices is related to the thickness of the cell, their number at the threshold depends upon the aspect ratio $\Gamma = R_1/e$, the ratio of the radius of the shear zone to the thickness of the cell.

In the original cell of RC we used mainly

$$R_1 = 4 \text{ cm} \quad e = 0.5 \text{ cm} \quad \Gamma = 8,$$

$$R_1 = 3 \text{ cm} \quad e = 0.3 \text{ cm} \quad \Gamma = 10,$$

$$R_1 = 4 \text{ cm} \quad e = 0.3 \text{ cm} \quad \Gamma = 13.3,$$

and

$$R_2 = 5.1 \text{ cm}.$$

With the new cell, the radius R_1 was either 6 cm or 9 cm (with $R_2 = 14$ cm) and the thickness could be chosen between $e = 0.3$ cm and $e = 1.5$ cm, so that values of Γ from 4 to 30 could be reached.

The fluid in the first cell was air and a mixture of water and glycerol in the second. In the latter case, the viscosity of the fluid could be tuned so that the accessible Reynolds number ranged from 5 to 3000.

In the previous work, we relied on visual observations. The cell was filled with air and a soap film was stretched in the central plane to give a precise visualization of the motion. The photographs in the present paper were taken using this technique. However, as noted in RC, this soap film shifts down slightly all the onset Reynolds values, and this shift also evolves in time as the soap film thins down. In the case of the glycerol solution, we could obtain a good visualization by introducing a few per cent of organic flakes commercially available under the name of 'Kalliroscope AQ 1000'. These flakes (6×30 μm^2 by 0.07 μm thick) become oriented along the flow, the reflected light then gives a visualization of the structure of the flow (Savas 1985; Matisse & Gorman 1984).

More precise data complementing the visualization were obtained by laser-Doppler anemometry. The fluid then had to contain dispersed particles. We used tobacco smoke in the air, and very dilute Kalliroscope in the water–glycerol solutions. The anemometry only measures one component of the velocity at one point of the laboratory frame. As simultaneous visualization was not always possible, we had to be able to deduce from the temporal laser measurement the spatial structure of the flow. As shown previously in RC in the stationary regime, the pattern of m vortices moves relative to the laboratory frame at an angular velocity Ω_v given by

$$\Omega_v = \alpha_m \Omega_1 + \beta_m \Omega_2,$$

Ω_1 and Ω_2 being the angular velocities of the inner and outer part of the cell respectively.

The values of α_m and β_m have been tabulated in RC for $m = 3$ to 8. Good empirical laws fitting all the observed values ($2 < m < 25$) are

$$\alpha_m = \tfrac{1}{2} - \frac{0.7}{m}, \quad \beta_m = \tfrac{1}{2} + \frac{0.7}{m}.$$

Note that the travelling velocity Ω_v differs from the mean velocity $\frac{1}{2}(\Omega_1 + \Omega_2)$ because of the geometrical deformation of the vortices along the circular shear (see RC).

When laser anemometry was used to study the velocity in a point near the

unstable region, the passing vortices modulated the local velocity so that their spatial periodicity was observed as a temporal periodicity of the anemometry signal. In the laboratory frame, the radial velocity is a periodic function of the polar angle θ

$$u_r(r,\theta) = u_0(r)\cos[m(\theta-\Omega_v t)].$$

The apparent frequency is then

$$f_0 = \frac{m}{2\pi}|\Omega_v| = \frac{1}{2\pi}|m\tfrac{1}{2}(\Omega_1+\Omega_2)+0.7(\Omega_2-\Omega_1)|,$$

where Ω_1 defines the positive direction. In stationary states, simultaneous measurements of Ω_1, Ω_2 and f_0 indicated which mode m was present in the cell even in the absence of visualization. The velocity signal was transformed by a spectrum analyser without any difficulty as our frequencies are not too low.

3. Experimental results

The present results complement the previous ones (RC). Particular attention will be given to the sequence of symmetry breaking, which creates successive stable states before a transition to a new regular mode.

3.1. *Primary instability*

The experimental procedure consists in increasing quasi-statically $\Delta\Omega = (\Omega_1-\Omega_2)$, the differential angular velocity between the inner and outer parts of the cell. The first destabilization changes the axisymmetrical flow into a pattern of vortices. Its onset is defined by a critical Reynolds number

$$Re_c = \frac{|\Delta\Omega|R_1 e}{\nu} \approx 80\pm 2.$$

The mode that appears is characterized by m_c, the number of vortices, or by the dimensionless wave vector

$$k_c e = m_c/\Gamma \approx 0.77\pm 0.03.$$

The measurements of $k_c e$ have been done in cells of large aspect ratio. For small Γ, the strong discretization conditions limits the possible modes, so the uncertainty $\pm 1/\Gamma$ becomes large.

This first transition has the characteristics of a supercritical bifurcation. Within the precision of our experiments, of the order of 1 %, there is no hysteresis, and the oscillatory part of the velocity signal corresponding to the vortices is proportional to $(Re-Re_c)^{\frac{1}{2}}$.

If the crossing of the threshold is not very slow, there is simultaneous nucleation of vortices in several zones along the shear, creating several groups of vortices of mean wave vector k_c. The initial pattern is then irregular and it takes a time T_s for the vortices to be phase correlated along the shear and for the pattern to be stable. This time T_s corresponds to a convective time, it increases with m_c and may be of the order of ten differential rotation times for $\Gamma = 30$.

For increasing values of the control parameter Re, successive transitions to modes with decreasing number of vortices, m, are observed. For decreasing values of Re, the reverse transitions occur with a large hysteresis. Figure 2 shows possible value of m in geometries where $\Gamma = 8$ or 13.3.

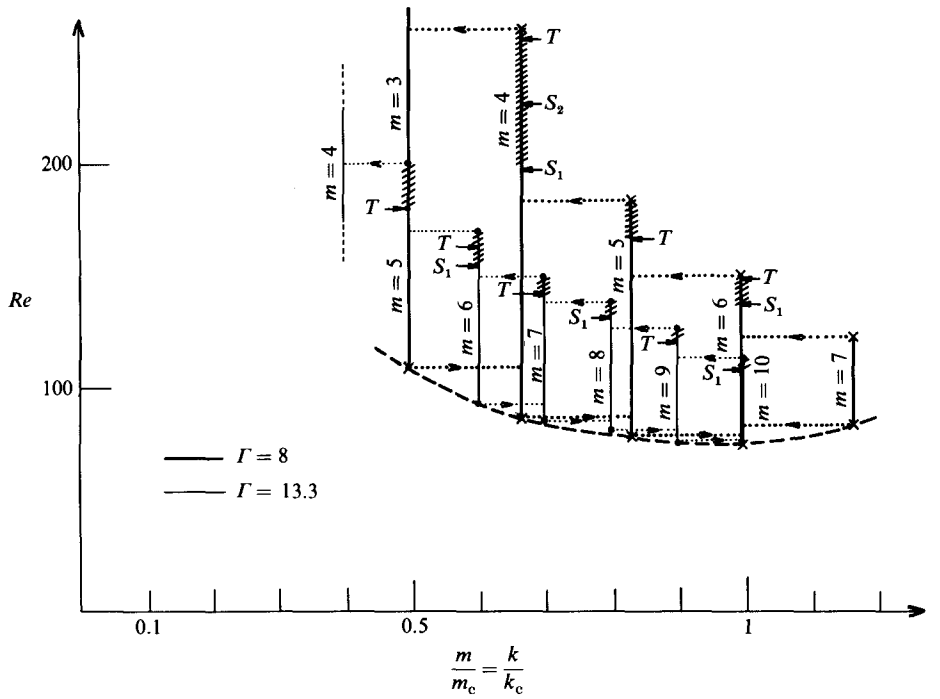

FIGURE 2. Domains of stability of the successive modes m in geometries of aspect ratio $\Gamma = 8$ and $\Gamma = 13.3$. The transition values, observed for increasing or decreasing Reynolds number, are shown. For example the mode $m = 5$ in $\Gamma = 8$ is stable from $Re = 80$ to $Re = 183$. Hatched lines represent the range where subharmonic modulation of the modes exist. (S_1 indicates the threshold of the first subharmonic mode, S_2 the threshold of the second subharmonic mode and T the threshold of the temporal mode.

3.2. *Lower marginal stability boundary*

The lower limit of stability of the modes, as the Reynolds number is decreased, is independent of the aspect ratio Γ of the cell. This can be seen in figure 2 or in figure 3 where the results obtained in three cells with $\Gamma = 6.5$, $\Gamma = 10$ and $\Gamma = 18$ are shown.

The marginal stability curve obtained by RC from a semi-quantitative model predicted correctly $k_c e$ but gave a value for the critical Reynolds number Re_c which was too small. The same model, but with a different estimate of the friction on the forcing walls, would give a similar curve (with the same value of $k_c e$) but a different Re_c. In this family of possible curves, we choose the one which fits the observed value $Re_c = 80$. It is drawn as a dashed line in the (Re, ke)-plane of figure 3. The experimental lower limits of stability of the modes are located extremely close to this curve. This also corresponds to the results of soap-film visualization (see figure 17 of RC). Before the transition m to $m+1$, the vortices become thin until one of them splits by a pinching of its elongated core. At this point their amplitude is very small and we reach the limits of our visualization and measurement techniques, so that it is not possible to get a more precise analysis in the experiment. We will see (§4.3) that in the numerical simulation the transition even occurs through an exchange of stability. The amplitude of the mode m vanishes so that a transitory axisymmetric mode can be seen briefly, which in turn give rise to a mode $m+1$ with a finite amplitude. Thus the lower limit of stability of the modes appears to be the marginal

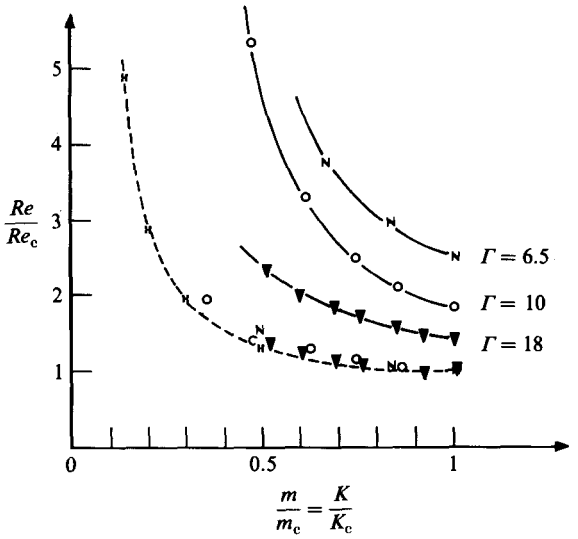

FIGURE 3. Upper and lower curve of stability for different value of Γ. The lower curves are all the same but the upper ones are all different. N, results of a numerical simulation with $\Gamma = 6.5$; O, experiment with $\Gamma = 10$; ▼, experiment with $\Gamma = 18$; ×, and – – – –, theoretical marginal stability curve.

stability curve itself. As transitions from m to $m+1$ vortices occur in a small range of Reynolds number where the vortices are very thin, we were not able to study more precisely the dynamics of the splitting of vortices.

Finally, in a few geometries ($\Gamma \approx 8$) an impulsive increase of $\Delta\Omega$ near the threshold sometimes creates an unlikely mode $m = m_c + 1$ with one more vortex than the critical mode obtained in the quasi-static case. This mode is then stable in a range of Reynolds number (figure 2). Either increasing or decreasing Re out of this range induces a transition to m_c and the lower limit of stability is again located on the marginal stability curve.

3.3. *Upper limit of stability of the modes*

For some of these measurements the Reynolds number may be large and then the results are not exactly the same rotating the inner part or the outer part faster. This must result from the amplification of three-dimensional recirculations. However all the experimental data given here for the upper limit of stability are obtained with no rotation of the outer part ($\Omega_2 = 0$).

The higher limit of stability of the modes depends strongly on Γ (in that respect, figure 10 of RC was erroneous as it was based on imprecise measurements by the soap-film technique in cells whose aspect ratios were too close to each other). Figure 3 shows that for large values of Γ the range of stability of each mode (distance between the upper curve and the lower curve) is narrow. In contrast, for small Γ, the stability range of a mode is large and the transition has different dynamics.

In large cells ($\Gamma > 10$) the number of vortices is larger near the threshold. With increasing Reynolds number, the transition from m to $m-1$ is abrupt and local. A fluctuation brings two vortices nearer to each other and they become unstable through pairing. The transition has no precursor and does not affect at first the other vortices of the pattern (figure 4). There is only an equilibration of the $m-1$ vortices along the shear after pairing.

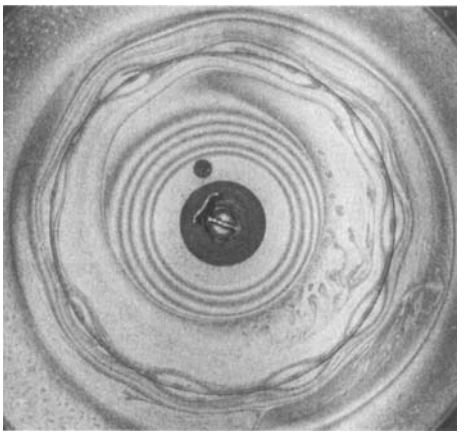

FIGURE 4. A transition by local pairing in a long chain of vortices. (Visualization by the soap-film technique).

In small cells ($\Gamma < 10$) discretization becomes a more dominant feature of the evolution. A mode can be forced and become unstable without the occurrence of pairing. Several successive precursor states exist near a transition, characterized by successive breaking of the spatial and temporal symmetries. We will describe them completely in two typical cases: $m = 4$ and $m = 5$. All the other possible situations for different values of m can be deduced by analogy.

3.3.1. *Evolution of an* ($m = 4$) *mode*

This case is particularly simple because of its fourfold symmetry. Figure 5 and 6 show the successive states of the flow as they are observed with the soap-film visualization (figure 5) and measured by Fourier transform of the local velocity signal (figure 6).

The initial state shown in figure 5(*a*) is a regular ($m = 4$) mode. The corresponding spectrum figure 6(*a*) only shows the frequency f_0 of passing vortices and its harmonics. Increasing the Reynolds number, when $Re = Re_1$, a first bifurcation occurs which changes the fourfold symmetry into a twofold symmetry. Two vortices become bigger and two smaller (figure 5*b*). This subharmonic modulation is steady in the vortices reference frame. The radial velocity in a point of the laboratory frame can be written as

$$u_r(r, \theta) = u_0(r) \cos[m(\theta - \Omega_v t)][1 + \epsilon \cos[\tfrac{1}{2}m(\theta - \Omega_v t)]].$$

The observed frequencies (figure 6*b*) are $\frac{1}{2}f_0$, f_0, $\frac{3}{2}f_0$ etc. The amplitude ϵ of the modulation grows as $(Re - Re_1)^{\frac{1}{2}}$ showing the supercritical character of this bifurcation. Figure 2 shows the range of stability of this modulated mode. At a second threshold Re_2 the remaining spatial twofold symmetry is in turn broken. All the vortices now have different sizes (figure 5*c*) and the spectrum (figure 6*c*) shows the frequency $\frac{1}{4}f_0$ and its combinations with the other frequencies. All the spatial symmetries are now broken, and the next transition breaks the temporal invariance. The size of each vortex fluctuates (this cannot be seen on the still photographs of figure 5*d* but is observed on videotape recordings). The spectrum (figure 6*d*) shows a new peak f_1 which is the first temporal frequency of the flow. Then a transient chaotic regime is observed, and transition to three regular vortices takes place (figure 5*d*).

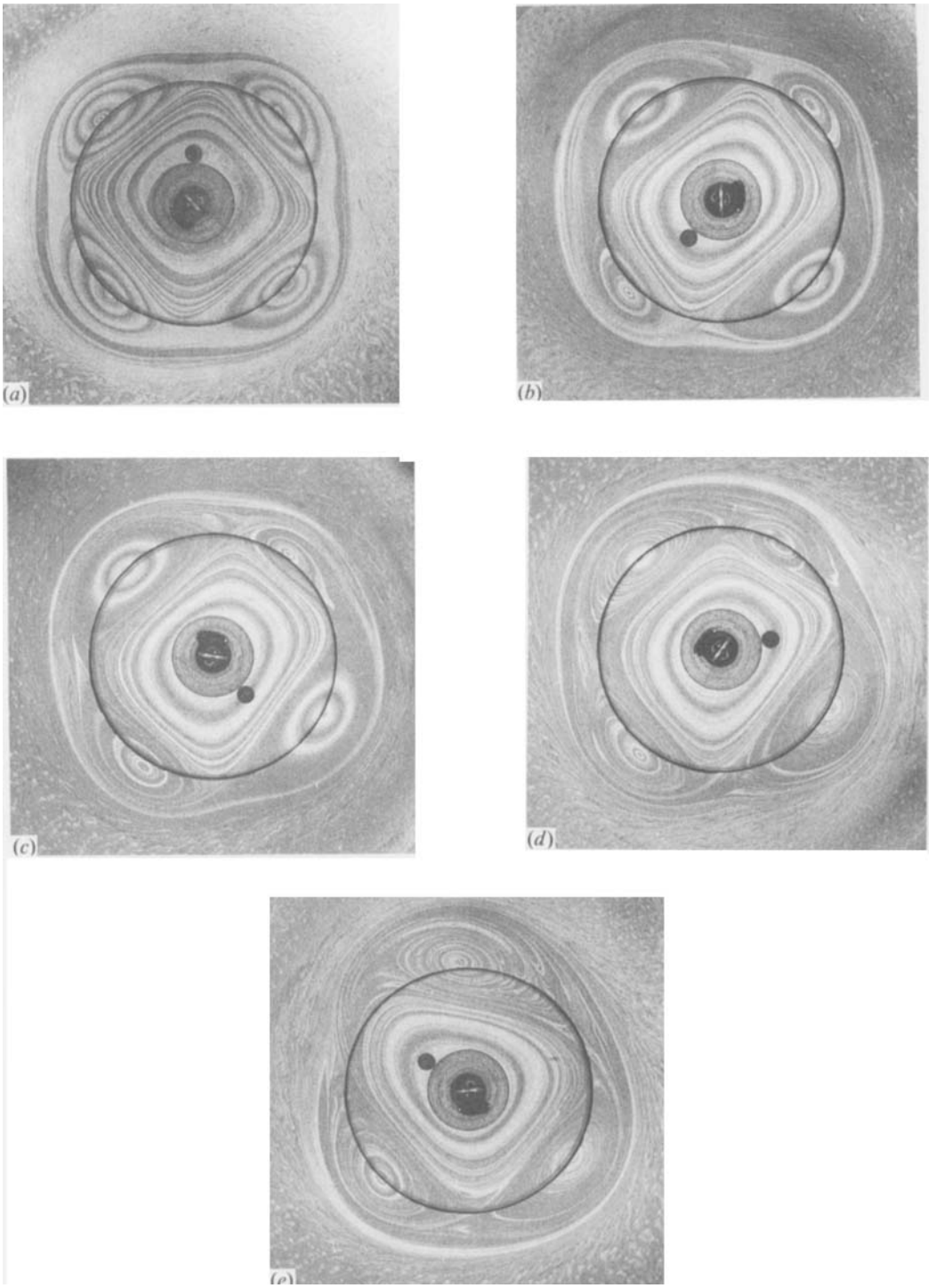

FIGURE 5. Five successive aspects of the vortex pattern before a transition $m = 4$ to $m = 3$ in a geometry $R_1 = 4$ cm, $e = 0.5$ cm and $\Gamma = 8$. (*a*) regular ($m = 4$) mode; (*b*) stationary mode with the first subharmonic modulation; (*c*) stationary mode with two subharmonic modulations; (*d*) temporal mode; (*e*) pattern just after the transition to $m = 3$.

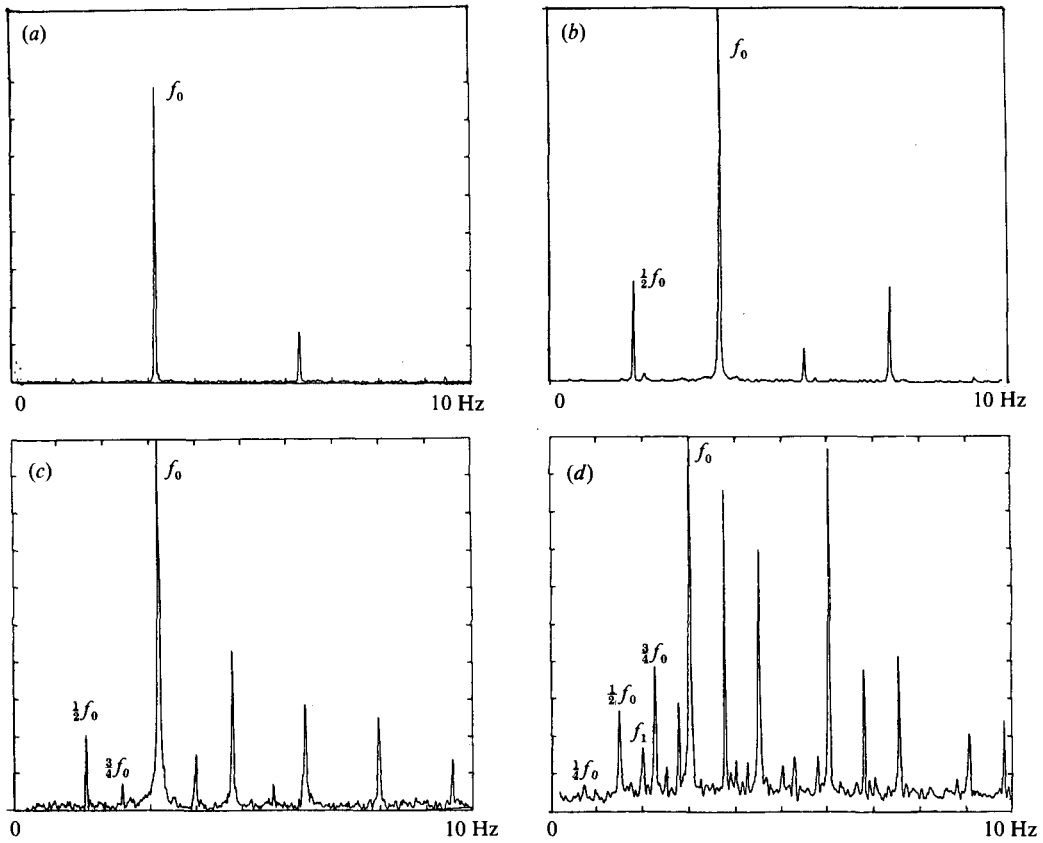

FIGURE 6. Four successive time spectra showing the spatial and then temporal frequencies in the states (*a*) to (*d*) shown in figure 5.

In summary, the initial spatial periodicity is broken by a series of supercritical transitions where successive subharmonics show up. This behaviour looks like a spatial analogue of the temporal subharmonic cascade (Maurer & Libchaber 1980; Feigenbaum 1978; Tresser & Coullet 1978). In this classical case the forcing of a nonlinear oscillator of fundamental period T leads to chaotic behaviour through a series of bifurcations where the periods $2T$, $4T$ etc. show up successively. If each bifurcation is characterized by the onset value of the control parameter μ_i there is a universal law

$$\lim \frac{\mu_i - \mu_{i-1}}{\mu_{i+1} - \mu_i} = \delta \approx 4.669.$$

In order for the analogy to be complete our threshold values Re_1, Re_2 ... etc. should show this behaviour. Unfortunately in the case $m = 4$ the number of possible subharmonics is not large enough to allow comparison, and in the case $m = 8$ the range in which subharmonics exist is extremely narrow and the measurements were not possible, so the issue remains undecided.

3.3.2. *Evolution of an* ($m = 5$) *mode*

The geometrical characteristics of the destabilization of the modes with a small odd number of vortices have already been discussed in RC. A more complete description can now be obtained with the help of both visualization of the pattern

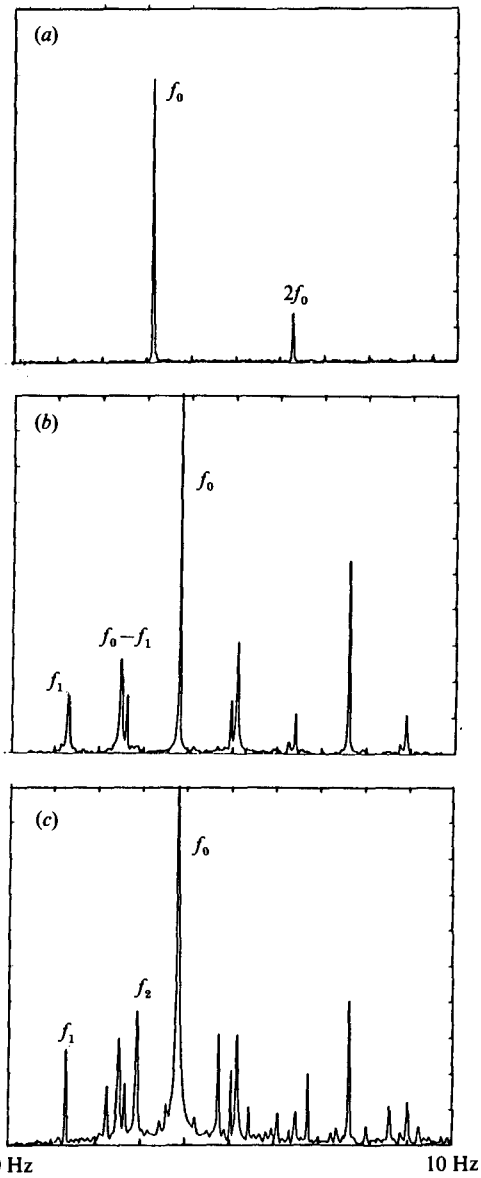

FIGURE 7. Three successive spectra in regular and modulated ($m = 5$) modes.

and measurement of the frequency spectrum. We will again choose here the notations introduced by Rand (1982) in his analysis of modulated waves in rotating systems and by Gorman, Swinney & Rand (1981) discussing results in Couette flow.

As the first subharmonic of an odd mode is not discretized along the circle, the first destabilization appears as a travelling wave which modulates the amplitude and the position of the vortices. On the spectrum several new peaks show up which we can label $f_1, f_0 - f_1, 2f_1$ etc. (figure 7*b*). As previously shown by RC, the pattern observed in the vortices reference frame at a time $t = 0$ is again observed at a time τ, but shifted by an angle $2\pi n/m$ (where $n = 2$) in the direction of the inner rotation Ω_1. At a time $m\tau$, the observed pattern is then identical to the initial state, so that $m\tau$ is the

temporal periodicity of the modulation in the vortex frame of reference. This period can be directly measured on videotape recordings.

The modulated velocity can be written

$$u_r(r,\theta) = u_0(r)\cos[m(\theta-\Omega_v t)]f(\theta,t).$$

We can change the angle θ for $\alpha = \theta-\Omega_v t$, so the new function $f(\alpha,t)$ is written in the vortices reference frame. The observed time τ corresponds to a periodicity conditions on f,

$$f(\alpha,t+\tau) = f\left(\alpha-2\left(\frac{2\pi}{m}\right),t\right).$$

The function f is also periodic in α and in t

$$f(\alpha+2\pi,t) = f(\alpha,t), \quad f(\alpha,t+m\tau) = f(\alpha,t),$$

so we can write its Fourier expansion

$$f(\alpha,t) = 1+\sum_l\sum_{l'}\epsilon(l,l')\cos[p_l(\alpha-\Omega_{l'}t)].$$

The three previous conditions on f give the equations

$$p_l = \tfrac{1}{2}(mk+k'),$$

$$p_l \in Z,$$

$$\Omega_{l'} = \frac{2k'\pi}{mp_l\tau}.$$

Then the first terms of the Fourier expansion are

$$f(\alpha,t) = 1+\epsilon'\cos(p'(\alpha-\Omega' t))+\epsilon''\cos(p''(\alpha-\Omega'' t))+\text{harmonics}\ldots$$

with $$p' = \tfrac{1}{2}(m+1), \quad p'' = \tfrac{1}{2}(m-1),$$

and $$\Omega' = \frac{4\pi}{m(m+1)\tau}, \quad \Omega'' = -\frac{4\pi}{m(m-1)\tau}.$$

As $\alpha = \theta-\Omega_v t$ and $f_0 = m\Omega_v/2\pi$, the fundamental frequencies of the modulation in the laboratory frame are

$$f' = \frac{p'(\Omega'+\Omega_v)}{2\pi} = \tfrac{1}{2}f_0+\frac{f_0}{2m}+\frac{1}{m\tau},$$

$$f'' = \frac{p''(\Omega''+\Omega_v)}{2\pi} = \tfrac{1}{2}f_0-\frac{f_0}{2m}-\frac{1}{m\tau}.$$

These two different travelling waves can account for the observed patterns. They correspond to the two nearest modes of the subharmonic of f_0. The first wave, associated to a quantification number $\frac{1}{2}(m-1)$ propagates in the negative direction (opposite to Ω_1), the other, associated to $\frac{1}{2}(m+1)$, propagates in the positive direction. RC attributed the observed modulation to the latter wave only. In fact the effects of these two waves are indistinguishable. Because they modulate localized vortices in m discrete points of a circle, their effect is identical. The nonlinearity of the phenomenon will generate any frequency combination of the basic f_0 frequency and the modulations frequencies. As f' and f'' verify, $f'+f'' = f_0$, it is readily seen

that the combinations of f' and f_0 are undistinguishable from the combinations of f'' and f_0. In figure 7(*b*) one can find the frequencies f_1, f_0-f_1, $2f_1$, f_0; where f_1 can be taken equal to $f'=f_0-f''$ or to f''.

In the range of existence of this vacillation state, the time τ is evolving and also depends on the value of m. It is also strongly dependent on the mean rotation $\frac{1}{2}(\Omega_1+\Omega_2)$ and we do not have a simple result on its evolution.

Still increasing the constraint, in a very narrow range of Reynolds number values, a second temporal frequency f_2 shows up in the spectrum (figure 7*c*), then a transition to a mode $m-1$ occurs.

3.3.3. *Evolution of the other modes*

As we have already stated, no subharmonic symmetry breaking has been seen for $m > 10$. The reason may be that the range of existence of this modulated state is less than the experimental resolution in the Reynolds number. For $m < 10$, before transition towards $m-1$ vortices, successive halving of the spatial symmetry occurs until an odd order symmetry is attained. Then a first and second temporal symmetry-breaking follows, before the transition to $m-1$ vortices. However the complete sequence is experimentally visible only for small value of m where the range of the cascade of bifurcation is large enough.

3.4. *Limit of stability for high value of Re*

Our interpretation of the experimental results relies on a certain number of assumptions. The limits of validity of these assumptions were only partially explored by RC and must be stated again.

In analysing the preceding results, we have always assumed that the centrifugal and Coriolis forces due to rotation could be neglected. This is only true when Ω_1 and Ω_2 are small so that the corresponding Ekman layer thickness $(\nu/\Delta\Omega)^{\frac{1}{2}}$ is larger than the thickness of the cell. This condition can be written $Re/\Gamma < 1$. Experimentally it is only when $Re/\Gamma > 20$ that disturbing effects appear. The growth of three-dimensional recirculation zones was noted earlier (RC figure 19). They are due to the action of inertial forces whenever the aspect ratio is small (strong curvature of the shear and large thickness of the cell). When $|\Omega_1-\Omega_2|$ is large, the thickness of the Ekman layers becomes smaller than e and toroidal recirculation regions show up and are superimposed on the original vortices and produce complicated three-dimensional structures.

Another limitation is linked to the mean rotation $\frac{1}{2}(\Omega_1+\Omega_2)$, which becomes strong when both rotation Ω_1 and Ω_2 are in the same direction. In this case the width of the horizontal shear tends to become limited by the Stewartson layer thickness (Stewartson 1957; Greenspan 1969) and no longer by the cell thickness. The resulting reduction of the width of the shear becomes apparent at the onset of the vortex formation. The critical Reynolds number Re_c is not affected but the number of vortices m_c increases steadily with the mean rotation. For instance m_c drifts from 10 to 15 in a cell where $\Gamma = 14$, when $\frac{1}{2}(\Omega_1+\Omega_2)$ changes from 0 to 10 times the threshold value $|\Omega_1-\Omega_2|_c$.

The third effect appears in all geometries when the Reynolds number is such that the number of vortices has been reduced to approximately half the initial value m_c. At this point the horizontal width of the vortices is much larger than the thickness of the cell. This triggers an instability of the vortex pattern, where little vortices constantly show up at the saddle points between the existing vortices, before pairing

with them. The number of vortices oscillates periodically. This effect is also observed in the numerical simulation where it appears also to be linked with the scale difference between the vortex size and the width of the forcing shear.

4. Numerical simulation

We are going to show that the main characteristics of the instability appearing in the laboratory experiment can be observed in a two-dimensional numerical simulation. We must however first discuss why, in our case, the experimental three-dimensional flow can realistically be simulated with a two-dimensional model.

In the following we take the origin 0 at the centre of the cell, $0z$ along the rotation axis, and $0xy$ in the middle plane of the cell. RC gave an analytical solution for the viscous flow problem in an infinite rectilinear analogue. They showed that in that case the velocity component along the vertical axis $0z$ vanishes although its horizontal components vary with z. The motion is horizontal with a three-dimensional variation in the vertical direction. In the circular geometry this is not strictly true, recirculation must exist but its velocity remains very small for large aspect ratio. RC also showed that the most unstable plane in the cell was the middle one where the width e' of the shear is maximum (of the order of e) and the wall dissipation minimum. Finally, the flow before and after its destabilization retains its symmetry with respect to the middle plane of the cell.

We are going to use these characteristics to simulate the dynamical properties of the flow in the middle plane and show their similarity with the experimentally observed instability.

4.1. *The equations of the motion*

The fluid velocity is $\boldsymbol{V}(u, v, w)$ and P the pressure. They satisfy the momentum equation and the continuity equation

$$\left.\begin{aligned} \frac{\partial \boldsymbol{V}}{\partial t} + (\boldsymbol{V}\cdot\boldsymbol{\nabla})\,\boldsymbol{V} = -\frac{1}{\rho}\boldsymbol{\nabla}P + \nu\nabla^2\boldsymbol{V}, \\ \boldsymbol{\nabla}\cdot\boldsymbol{V} = 0, \end{aligned}\right\} \tag{1}$$

with no-slip conditions on the horizontal and vertical boundaries of the cell

$$\boldsymbol{V}(x, y, \pm\tfrac{1}{2}e) = \boldsymbol{V}_{\mathrm{b}}(x, y),$$

$$\boldsymbol{V}(x^2 + y^2 = R_2^2) = (-y\Omega_2, x\Omega_2, 0),$$

where $\boldsymbol{V}_{\mathrm{b}}$ is the velocity on the top and bottom walls (figure 1). From the symmetry with respect to the $x0y$-plane we deduce

$$w(z = 0) = 0, \qquad \frac{\partial^2 w(z = 0)}{\partial z^2} = 0,$$

$$\frac{\partial \boldsymbol{V}_{\mathrm{h}}(z = 0)}{\partial z} = 0, \qquad \frac{\partial P(z = 0)}{\partial z} = 0,$$

where $\boldsymbol{V}_{\mathrm{h}}$ is the horizontal projection of $\boldsymbol{V}$.

In the median plane, the equations (1) reduce to

$$\frac{\partial \boldsymbol{V}_h}{\partial t}+(\boldsymbol{V}_h\cdot\boldsymbol{\nabla}_h)\,\boldsymbol{V}_h=-\frac{1}{\rho}\boldsymbol{\nabla}_h P+\nu\nabla_h^2\,\boldsymbol{V}_h+\nu\frac{\partial^2 \boldsymbol{V}_h}{\partial z^2}, \tag{2a}$$

$$\boldsymbol{\nabla}_h\cdot\boldsymbol{V}_h+\frac{\partial w}{\partial z}=0, \tag{2b}$$

$$w=0, \tag{2c}$$

where $\boldsymbol{\nabla}_h$ and ∇_h^2 are respectively the horizontal gradient and horizontal Laplacian operators. These equations differ from the two-dimensional Navier–Stokes equations only by the last term on the right-hand side of (2*a*) and the last term on the left-hand side of (2*b*).

In the continuity equation (2*b*) the term $\partial w/\partial z$ shows the possibility of horizontal divergence due to three-dimensional recirculations. Dimensional analysis and observation show that this term is small and we will neglect it.

In the momentum equation, the last term represents the drag in the central plane due to the friction on horizontal walls. This forcing term, that we will denote as $\boldsymbol{F}$, has to be modelled in order to obtain a closed set of equations. The more natural assumption, as soon as the fluid motion differs from solid-body rotation, is to assume, for the velocity, a parabolic vertical dependence characteristic of Poiseuille flow between two planes; then (from now on we will write $\boldsymbol{V}$ instead of $\boldsymbol{V}_h$)

$$\boldsymbol{F}=\nu\frac{\partial^2 \boldsymbol{V}}{\partial z^2}\approx\frac{8\nu}{e^2}(\boldsymbol{V}_b-\boldsymbol{V}),$$

where $\boldsymbol{V}_b$ is the boundary velocity on top or bottom walls. However, $\boldsymbol{V}_b$ cannot be used in the simulation because it is a discontinuous function of the radial distance to the rotation axis. RC had shown that the typical width of the shear (in the middle plane of the cell) is equal to the cell height e. In order to get around the difficulty due to the discontinuity of $\boldsymbol{V}_b$, we make a rather crude approximation by replacing $\boldsymbol{V}_b$ by a continuous velocity $\boldsymbol{V}^*$ with a piecewise linear profile of width e. This approximation certainly affects the instability threshold observed in the simulation. However, after the vortices have formed the experiment shows that the shear width becomes much larger than e. As a result the approximation should become much better over the threshold; then the difference between the forcing by $\boldsymbol{V}_b$ or by the model $\boldsymbol{V}^*$ probably vanishes. The forcing term is now

$$\boldsymbol{F}=\frac{8\nu}{e_2}(\boldsymbol{V}^*-\boldsymbol{V}),$$

with

$$\boldsymbol{V}^*=\Omega_1 r\,\boldsymbol{e}_\theta \quad \text{for } 0<r<R_1-\tfrac{1}{2}e,$$

$$\boldsymbol{V}^*=\left[\Omega_1+(\Omega_2-\Omega_1)\left(\frac{r-R_1+\frac{1}{2}e}{e}\right)\right]\boldsymbol{e}_\theta \quad \text{for } R_1-\tfrac{1}{2}e<r<R_1+\tfrac{1}{2}e,$$

$$\boldsymbol{V}^*=\Omega_2 r\,\boldsymbol{e}_\theta \quad \text{for } R_1+\tfrac{1}{2}e<r<R_2,$$

where $\boldsymbol{e}_\theta$ is the azimuthal unit vector.

Introducing the stream function ψ and the vorticity ω, equations (2) become

$$\frac{\partial\omega}{\partial t}+\mathrm{J}(\psi,\omega)=\nu\nabla^2\omega-\frac{8\nu}{e^2}(\psi-\psi^*), \tag{3}$$

$$\nabla^2\psi=\omega,$$

where $J(\psi, \omega)$ is the Jacobian operator

$$J(\psi, \omega) = \frac{\partial \psi}{\partial x}\frac{\partial \omega}{\partial y} - \frac{\partial \psi}{\partial y}\frac{\partial \omega}{\partial x},$$

and ψ^* the stream function of $\boldsymbol{V}^*$

4.2. *The numerical code*

The numerical code was adapted to the present geometry from a pseudo-spectral Fourier code previously used for homogeneous two-dimensional turbulence studies (Basdevant *et al.* 1981).

In the pseudo-spectral Fourier method, the flow is supposed to be 2π-periodic in x- and y-directions; the velocity is then evaluated at the nodes of a 128×128 regular grid covering the basic square $[0, 2\pi[\times [0, 2\pi[$. The Jacobian is calculated on this square. Evaluation of any partial derivative at the same points is performed through spectral decomposition of the function. The solution of the Laplace problem is obtained in the same way. The program then involves back and forth transforms between physical space and spectral (Fourier) space; these transforms are conducted very efficiently by means of fast Fourier transforms (FFT). Several problems arise and these are detailed in §§4.2.1–4.2.5.

4.2.1. *Sub-grid motion modelling*

As we are working on a discrete grid, scales smaller than the mesh size cannot be calculated. Because of the nonlinear terms, however, all the scales are linked, so that we need to dissipate the subgrid scales in such a way that the larger scales are not affected. It was shown by Basdevant & Sadourny (1983) that this can be done by replacing the dissipative term $\nu\nabla^2\omega$ in (3) by a superdissipative one:

$$-\frac{1}{T k_{\max}^{2p}} (\nabla^2)^p(\omega),$$

where T is the turnover time of the small-scale motion and $k_{\max}$ the largest wave vector in the Fourier space. For $p = 8$ and with a 128×128 model, this operator dissipates the enstrophy (spatial integral of the square of the vorticity) at the mesh scale without otherwise disturbing the flow in other scales. Coherence in the spatial and temporal resolution is obtained by choosing the calculation's timestep Δt of the order of T. In any case the linear dissipation of equation (3)

$$\frac{8\nu}{e^2}(\psi - \psi^*)$$

dominates, and it would only be at very large Reynolds number that these cautions would be important.

4.2.2. *Geometry*

Both the shear and the external walls of the cell are circular, while in the simulation the physical space is represented by a square with periodic boundaries. We apply a no-slip condition on a circle of radius R_2 with a mask method (Basdevant & Sadourny 1983). At each timestep, the velocity field in the real space is set to be zero outside a circle of radius R_2. This does not disturb the flow if R_1 is not too near R_2. In practice, we chose $R_2 = 60$ grid meshes and R_1 was always smaller than 40. This method is simple but requires that the external part of the shear has no rotation ($\Omega_2 = 0$), otherwise the stability condition would impose too small a timestep.

4.2.3. *Symmetry*

The first numerical simulations only showed modes with $m = 8$ or 4 vortices. The reason was that a point of the grid had been taken as the centre of the cell. The resulting fourfold symmetry imposed itself on the vortex pattern. A small shift of the centre so that it no longer coincided with a point of the grid was enough to suppress this spurious effect.

4.2.4. *Computation time*

The computation was done on an array processor (AP 120) with a peak power of 12 M.Flops. One timestep required 1.5 s of calculation so that one period of rotation of the central part of the cell requires about 10 min of calculation. For this reason, the search for stationary states was long and we will describe later by which indirect method the instability threshold could be determined.

4.2.5. *Outputs*

We will draw the vorticity field because of its visual similarity with the patterns observed with the soap-film technique. We can also draw the time evolution of one component of the velocity at one point and compute its power spectrum, as in the experiment.

4.3. *Numerical results*

Before describing the results of the numerical simulation, we must discuss the possibility of comparison with experiments. The numerical circular shear zone can be characterized by the numerical aspect ratio Γ_{num}, the ratio of its radius to its width

$$\Gamma_{\text{num}} = R_1/e,$$

which is equivalent to the experimental aspect ratio Γ.

The definition of a numerical Reynolds number is more difficult. In the plane of the shear, the viscosity has been replaced by a superdissipativity which could seem to make the Reynolds number irrelevant. However, the forcing of the flow by

$$\boldsymbol{F} = \frac{8\nu}{e^2}(\boldsymbol{V}^* - \boldsymbol{V}),$$

introduces a parameter $N = 8\nu/e^2$ which depends upon both the viscosity of the fluid and the thickness of the cell. N is a parameter we can tune in the numerical simulation. A numerical Reynolds number can be written

$$Re_{\text{num}} \approx \frac{R_1 e \Omega_1}{\nu} = \frac{8\Omega_1 \Gamma_{\text{num}}}{N}.$$

However, it must be kept in mind that the numerical factor 8 comes from a rough estimate so that exact quantitative agreement between the numerical and experimental values should not be expected.

4.3.1. *The instability threshold*

For low angular velocity Ω_1, the vorticity lines remain at first circular (figure 8). Then, with increasing Ω_1, a mode with m_c vortices appears. Changing the aspect ratio Γ_{num} from 5 to 20, we found m_c to be related to Γ_{num} by

$$m_c = (0.95 \pm 0.15)\,\Gamma_{\text{num}},$$

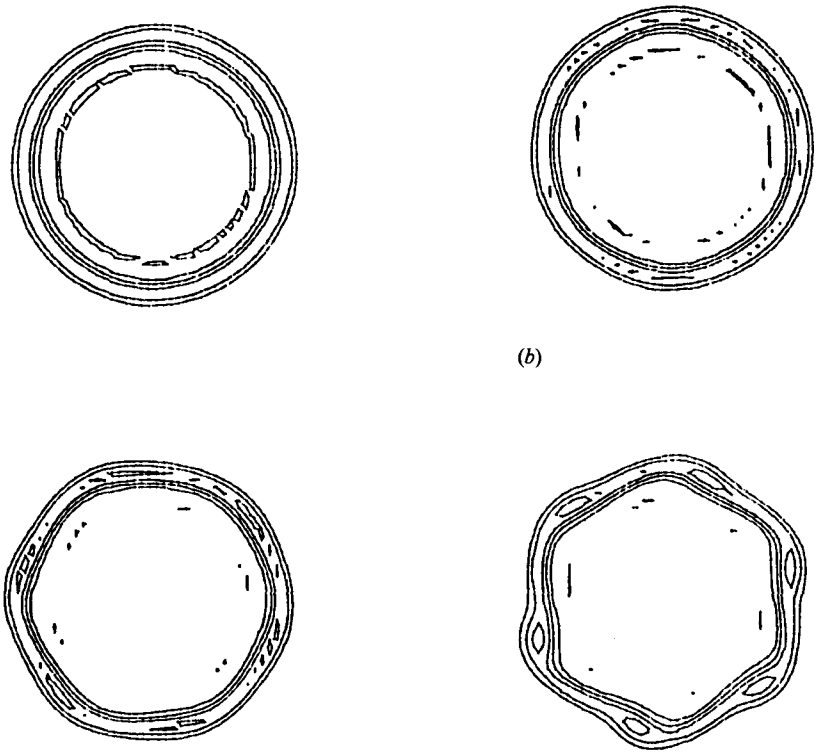

FIGURE 8. Crossing the instability threshold in the numerical simulation ($\Gamma_{\text{num}} = 6.5$). Figures (a)–(d), represent successive pictures of the time evolution of the flow after an impulsive increase of the forcing.

while in the experiment, we had

$$m_c = (0.77 \pm 0.03)\,\Gamma.$$

The discrepancy is due to the uncertainty in the width definition of the shear which is only a few mesh points thick in the numerical model.

The technique by which the threshold is determined in the laboratory experiment (quasi-static increase of the stress) is impossible to use here because the computing time it would require would be too large. We use a different method. Experimentally, the bifurcation was supercritical; assuming here the same characteristic, we use the corresponding amplitude equation

$$\frac{\partial A}{\partial t} = \sigma(\mu)\,A - \beta\,|A^2|\,A,$$

where A is the amplitude of the velocity, for instance the radial velocity created by the vortices, $\sigma(\mu)$ the growth rate, $\mu = Re - Re_c$ is the distance to the threshold. Near the threshold, $A = A_0 \exp[\sigma(\mu)t]$ and $\sigma(\mu)$ is proportional to μ. The time τ needed for the signal to reach a given amplitude A_1 (e.g. 10 times the noise amplitude A_0) is inversely proportional to μ,

$$\tau \sim \frac{1}{\sigma(\mu)} \sim \frac{1}{\mu}.$$

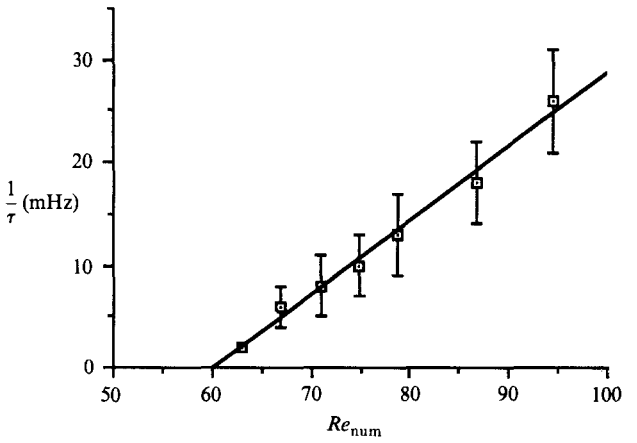

FIGURE 9. The extrapolation method giving the onset of the instability. $Re_c \approx 60$ in a geometry where $\Gamma = 6.5$.

Figure 9 shows a plot of τ^{-1} as a function of Re_{num}. Its extrapolation to $\tau^{-1} = 0$ gives, with a good precision, the critical value $(Re_{num})_c$ at the threshold. The corresponding value of the numerical Reynolds number is

$$Re_{num} \approx 55 \pm 10.$$

For the reasons previously discussed, the discrepancy with the experiment ($Re_c \approx 80$) is not surprising.

As in the experiment, a further increase of Ω_1 leads in the simulation to successive transitions to modes with decreasing values of m. For each mode, the travelling velocity of the vortices is the same as in the experiment and given by

$$\Omega_v = \left(\frac{1}{2} - \frac{0.7}{m}\right)\Omega_1 \quad (\Omega_2 = 0).$$

4.3.2. *Lower limit of stability of the modes*

A decrease of Ω_1 produces the reverse transitions with a very strong hysteresis. Figure 10 shows a series of drawings in which a mode $m = 3$ undergoes transition to $m = 5$. The vortices become very elongated, then the mode $m = 3$ disappears, a transitory axisymmetric flow appears which is itself unstable and gives rise to the mode $m = 5$. In this case, the return transitions seem to occur also on the marginal stability curve. This situation apparently differs from the experiment where transition occurs through the splitting of elongated vortices. The chosen piecewise model of the velocity profile might be responsible for this behaviour of the numerical simulation.

4.3.3. *Upper limit of stability of the modes*

As in the experiment, the transitions under increasing stress have characteristics which depend upon the aspect ratio Γ_{num}. For larger values, localized pairings occur. For small values, $\Gamma_{num} < 8$, a series of bifurcations corresponding to successive breakings of symmetries of the vortex pattern occur before transition to a mode of smaller m. Figure 11 shows the range of stability of the modes in a case where $\Gamma_{num} = 6.5$. Although less precise, this figure can be compared to figure 2.

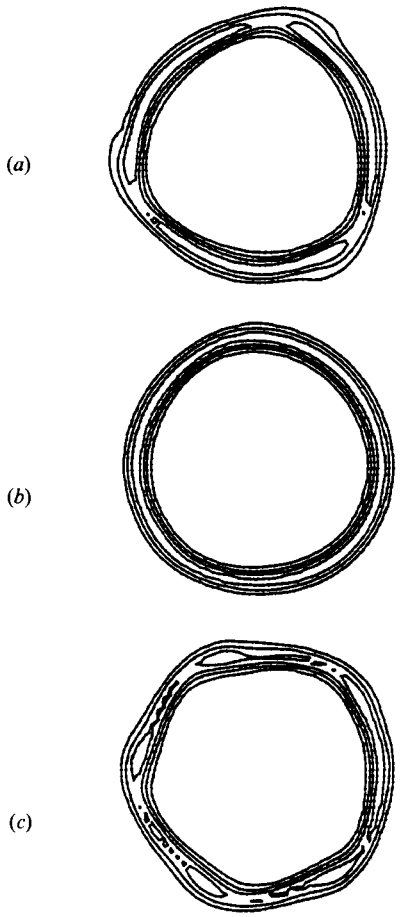

FIGURE 10. Transition between $m = 3$ and $m = 5$ for a decreasing constraint. $\Gamma = 6.5$ and $Re = 1.5\ Re_c$.

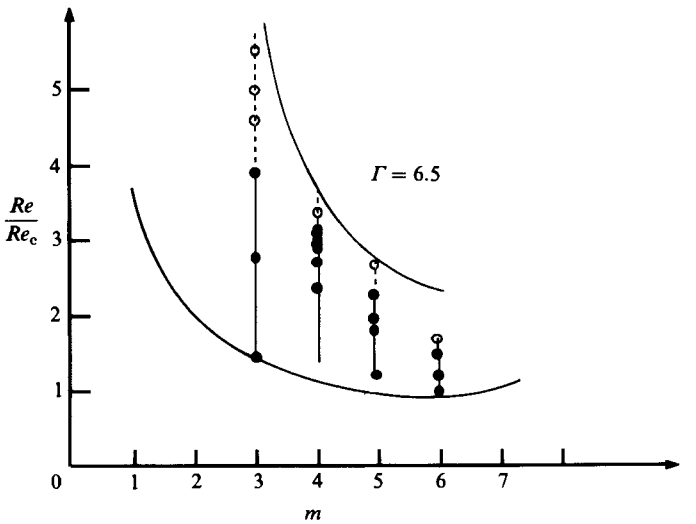

FIGURE 11. Stability domains of the successive modes in the two-dimensional simulation in a geometry corresponding to $\Gamma = 6.5$ (to compare with figure 2). ●, stable regular states obtained in that geometry; ○, stable modulated states.

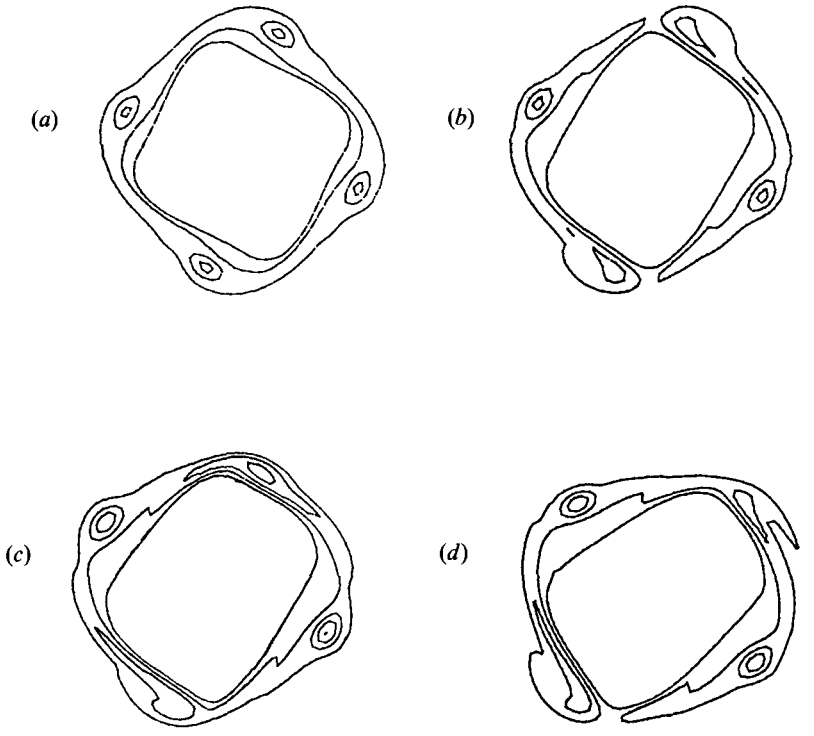

FIGURE 12. Four successive states of an ($m = 4$) mode obtained by numerical simulation. (*a*) regular; (*b*) first stationary modulation; (*c*) second stationary modulation; (*d*) first temporal modulation.

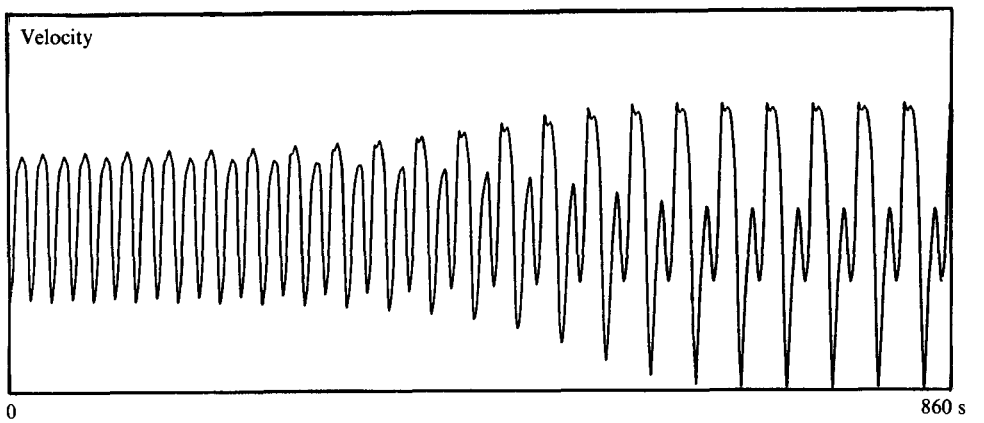

FIGURE 13. The direct velocity signal showing the growth of the subharmonic amplitude and its saturation in time.

Case $m = 4$

The sequence of symmetry breaking in the case of $m = 4$ is shown in figure 12. The evolution is identical to the experimental one shown in figure 5. Figure 13 shows the radial velocity measured at one point as a function of time when a slow increase of Ω_1 produces the bifurcation to a state modulated by a first spatial subharmonic.

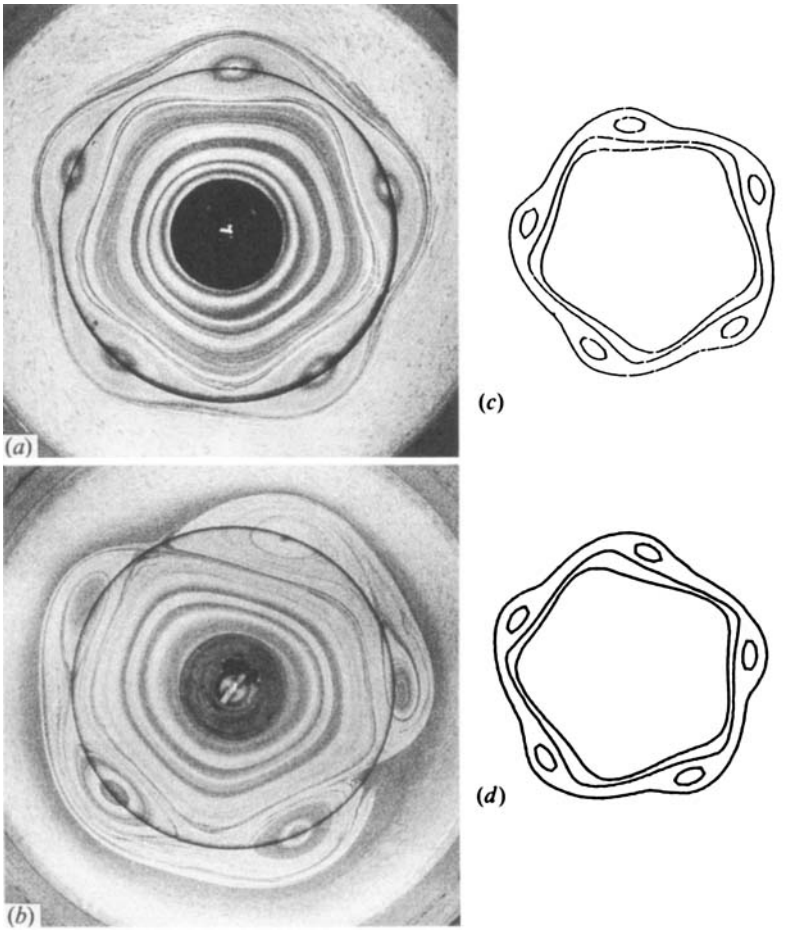

FIGURE 14. Comparison of observed patterns of a mode $m = 5$ in the experiment and in the simulation.

Case $m = 5$

In the case $m = 5$, a travelling wave shows up which modulates the amplitudes of these vortices. Figure 14 shows a comparison of the pattern observed experimentally and numerically. The power spectrum of the modulated state is shown in figure 15. It can be compared to the experimental one shown on figure 7(*c*). The resolution in the numerical spectrum is poor due to the very small acquisition time compared to the evolution time available in the experiment. For this reason the second temporal frequency f_2, which appears in the experiment, is not observed numerically.

4.3.4. *Limitation at high values of Re*

Increasing the rotation of the inner part we observe modes with fewer and fewer vortices. For example in the geometry where $\Gamma = 6.5$ we observe a minimum of $m = 3$ vortices. Further increase of the Reynolds number ($Re > 20\ Re_c$) could not be done because the stability of the simulation demands very small values of the timestep.

In the simulation as in the real experiment, when m is less than or equal to $\frac{1}{2}m_c$ the

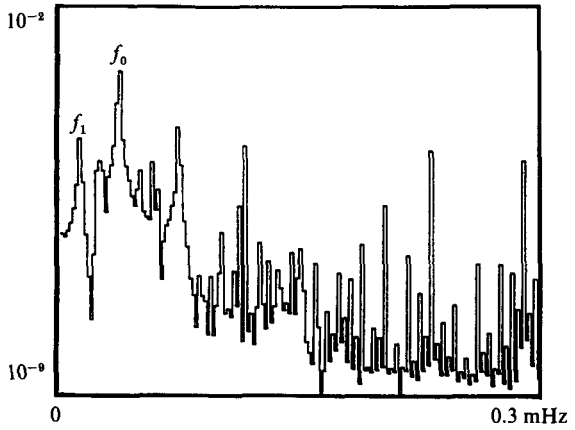

FIGURE 15. The logarithmic velocity spectrum in a point of the simulation grid, for a modulated $m = 5$ mode.

evolution laws are changed and no more stable or well-defined patterns exist. The two scales, vortex diameter and thickness of the original shear zone, seem now to be too different to give stationary solutions.

5. Conclusion

In the conclusion we can now return to the various growth types of instabilities. The distinction between convective and absolute instability is very clear in the case of mixing layers (or jets), because the splitter plate (or the nozzle) at the end of which the fluids meet, singles out the laboratory frame of reference. Galilean invariance is broken and it is in the laboratory frame that the group velocities of the perturbation have to be compared to the mean advection velocity. However this comparison is meaningless in flow where a translational invariance would exist.

In our experiment we do not have translational invariance but, along the shear, we do have rotational invariance. We have shown that, in the range of velocities in which we work, the specific forces due to rotation can be neglected. As a result the various rotating frames of reference are practically as undistinguishable as Galilean frames. (There would be Galilean invariance in the linear analogue introduced by RC). For this reason the distinction between convective and absolute instability loses its meaning here. As noted previously the same patterns will be observed whether the two rotations Ω_1 and Ω_2 are of the same direction or not. Because of the invariance the distinction between convective and absolute instability has no meaning here. We could better describe our case as a spatially periodic flow. This type of instability, even though it does not have the same symmetries, has most of the characteristics of the absolute unstable flows because we can conveniently choose the frame of reference in which the vortices are motionless and describe their growth as a temporal process.

The difference with the convective case can be illustrated by a side experiment where we broke the rotational invariance of our cell. As shown in figure 16 we placed a metallic grid across the shear zone. This grid was maintained motionless in the laboratory frame. It was easily crossed by the fluid but broke the vortices when the flow traversed it. In the case shown on the photograph there is no external rotation ($\Omega_2 = 0$). The flow then becomes somewhat similar to that of a mixing-layer

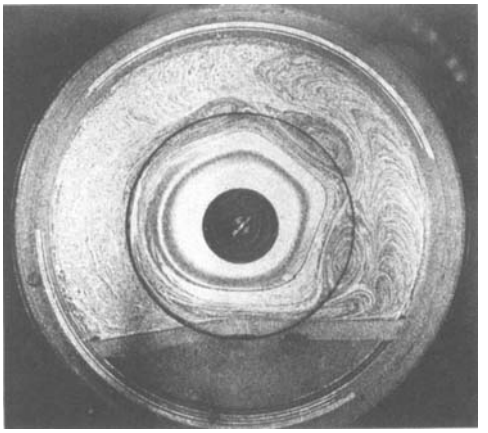

FIGURE 16. Photograph of the flow in a cell with broken symmetry (for $\Omega_2 = 0$).

experiment. The vortices show up downstream from the grid, they grow in size then disappear when they hit the grid again. There was no stationary mode in this case nor regularity in the flow as the instability had been brought back to a convective one. Had it been possible to have $\Omega_2 \neq 0$ without the grid rotating, we could have obtained absolute instability in this cell with broken symmetry.

Coming back to the geometry we used in the present article we notice that it is very close to the numerical simulations of an homogeneous linear shear with periodic conditions. In large cells the flow reorganizes in a regular mode in a time which grows with the aspect ratio. One may wonder what the behaviour of the instability would be if the periodicity (length of the perimeter) tended to infinity so as to relax the periodicity conditions. Presumably, at the threshold, there would be initial germination of vortices in independent regions along the shear. These would spread and form independent wave packets with phase jumps between them. In very large cells the constraint due to the periodicity would be slow in destroying these defects. For similar reasons the evolution of the flow at higher Reynolds number depended also upon the aspect ratio of the cell. In all cases, with the increase of the constraint, the vortices tend to grow and the basic local process is their pairing. For a large number m of vortices (which corresponds to large aspect ratio Γ) the transition to $(m-1)$ occurs abruptly and is local in space. In contrast, transitions of patterns with few vortices ($m < 10$) are strongly limited by geometrical constraints. They occur after a series of bifurcations which correspond to the breaking of the spatial and temporal symmetries of the flow.

The general features of such a series of symmetry breaking was studied by Rand (1982) from a mathematical point of view. As RC pointed out, the states of the system that we observe all enter his classification of possible rotating flow. Other cases of sequences of spatial and temporal symmetry-breaking are observed in other systems which have rotational invariance. The two nearest are the Taylor Couette flows (Gorman *et al* 1981) and the convection flow in rotating cylinders (Hide & Mason 1975; Hignett 1985). However these two systems are more complex than ours because the instabilities are fully three-dimensional, the forces characteristic of rotation are present and the number of control parameters is larger. In the present experiment the basic flow is three-dimensional, but we showed that all the observed

dynamical characteristics of our laboratory experiments are also observed in a two-dimensional numerical model. We must emphasize that the numerical simulation does not claim to be completely realistic. It is all the more interesting that both the experimental and the numerical simulation show the same dynamical behaviour, because they pertain to a more general class; they illustrate the possible sequence of bifurcations where a continuous group of rotational symmetry is broken by a two-dimensional instability.

High mechanical precision in our experimental cells could only be obtained by ingenious design due to H. Thomé. We are also grateful to J. Brochard and J. Meunier for their care in the manufacturing of these cells, and to Mrs Philippe who constantly helped us with the numerical simulation. Effects of a strong mean rotation on the observed patterns was studied by P. Valentin during a training period. We thank P. Huerre for stimulating discussions.

REFERENCES

AREF, A. 1983 Integrable, chaotic and turbulent vortex motion in two-dimensional flows. *Ann. Rev. Fluid Mech.* **15**, 345.

BASDEVANT, C., LEGRAS, B., SADOURNY, R. & BÉLAND, M. 1981 A study of barotropic model flows: intermittency, waves and predictability. *J. Atmos. Sci.* **38**, 2305.

BASDEVANT, C. & SADOURNY, R. 1983 Modélisation des échelles virtuelles dans la simulation numérique des écoulements turbulents tridimentionnels. *J. Méc.* Special number, p. 243.

FEIGENBAUM, M. J. 1978 Quantitative universality for a class of nonlinear transformations. *J. Stat. Phys.* **19**, 25.

GORMAN, M., SWINNEY, H. L. & RAND, D. A. 1981 Doubly periodic circular Couette flow: experiments compared with predictions from dynamics and symmetry. *Phys. Rev. Lett.* **46**, 992.

GREENSPAN, H. P. 1969 *The Theory of Rotating Fluids*, p. 100. Cambridge University Press.

HIDE, R. & MASON, P. J. 1975 Sloping convection in a rotating fluid. *Adv. Phys.* **24**, 47.

HIGNETT, P. 1985 Characteristics of amplitude vacillation in a differentially heated rotating fluid annulus. *Geophys. Astrophys. Fluid Dyn.* **31**, 247.

HUERRE, P. & MONKEVITZ, P. A. 1985 Absolute and convective instabilities in free shear layers. *J. Fluid Mech.* **159**, 151.

HO, C. M. & HUANG, L. S. 1982 Subharmonics and vortex merging in mixing layers. *J. Fluid Mech.* **119**, 443.

HO, C. M. & HUERRE, P. 1984 Perturbed shear layers. *Ann. Rev. Fluid Mech.* **16**, 365.

LAMB, H. 1932 *Hydrodynamics*, 6th edn, chapter 7. Dover.

MATISSE, P. & GORMAN, M. 1984 Neutrally buoyant anisotropic particles for flow visualization. *Phys. Fluids* **27**, 759.

MAURER, J. & LIBCHABER, A. 1980 Effect of the Prandtl number on the onset of turbulence in liquid ^{4}He. *J. Phys. Lett. Paris* **41**, L. 515.

PIERREHUMBERT, R. T. & WIDNALL, S. E. 1982 The two- and three-dimensional instabilities of a spatially periodic shear layer. *J. Fluid Mech.* **114**, 59.

RABAUD, M. & COUDER, Y. 1983 A shear-flow instability in a circular geometry. *J. Fluid Mech.* **136**, 291.

RAND, D. 1982 Dynamics and symmetry. Predictions for modulated waves in rotating fluids. *Arch. Rat. Mech. Anal.* **59**, 1.

SAVAŞ, Ö. 1985 On flow visualization using reflective flakes. *J. Fluid Mech.* **152**, 235.

STEWARTSON, K. 1957 On almost rigid rotations. *J. Fluid Mech.* **3**, 17.

STUART, J. T. 1967 On finite amplitude oscillations in laminar mixing layers. *J. Fluid Mech.* **29**, 417.

THORPE, S. A. 1971 Experiments on the instability of stratified shear flows: miscible fluids. *J. Fluid Mech.* **46**, 299.

TRESSER, C. & COULLET, P. 1978 Itérations d'endomorphismes et groupes de renormalisations. *C. R. Acad. Sci. Paris* **287** A, 577.

WINANT, C. D. & BROWAND, F. K. 1974 Vortex pairing: the mechanism of turbulence mixing layer growth at moderate Reynolds number. *J. Fluid Mech.* **63**, 237.